Citation (APA)
Fotouhi, M., Assaad, M., Imran, A., & Bodaghi, M. (2026). A lightweight mechanical metamaterial framework produced via 3D printing for next-generation dental implants. *Journal of Materials Research and Technology*, *44*, 3015-3029.
https://doi.org/10.1016/j.jmrt.2026.08.198

Journal of Materials Research and Technology 44 (2026) 3015–3029

Contents lists available at ScienceDirect

Journal of Materials Research and Technology

journal homepage: www.elsevier.com/locate/jmrt

A lightweight mechanical metamaterial framework produced via 3D printing for next-generation dental implants

Mohammad Fotouhi [a,*], Maher Assaad [b], Ahmed Imran [c], Mahdi Bodaghi [d]

[a] Faculty of Civil Engineering and Geosciences, Delft University of Technology, 2628 CD, Delft, the Netherlands
[b] Department of Electrical and Computer Engineering, College of Engineering and IT, Ajman University, P.O. Box 346, Ajman, United Arab Emirates
[c] Department of Biomedical Engineering, College of Engineering and IT, Ajman University, P.O. Box 346, Ajman, United Arab Emirates
[d] Department of Engineering, School of Science and Technology, Nottingham Trent University, Nottingham, NG11 8NS, UK

ARTICLE INFO

Keywords:
Triply periodic minimal surface (TPMS)
3D printing
Lightweight metamaterial
Parametric design
Compression deformation

ABSTRACT

Lightweight mechanical metamaterials have attracted increasing attention due to their ability to achieve unusual mechanical properties through architectural design rather than chemical composition. In this study, a novel cylindrical metamaterial based on a gyroid triply periodic minimal surface (TPMS) architecture is proposed, selected for its high strength-to-weight ratio, smooth stress distribution, and fully interconnected porosity that are advantageous for load-bearing biomedical applications. A combined experimental and numerical approach was employed, where the finite element model was validated against quasi-static compression tests conducted on 3D-printed specimens (1.9 mm thickness, eleven unit-cells). The validated model achieved excellent agreement with experiments (R2 = 0.965), capturing the two-phase deformation behavior: an initial elastic regime followed by plasticity-driven global buckling initiating at the core between neighboring unit-cells. A comprehensive parametric study was then performed to investigate the effects of unit-cell wall thickness (1.1–2.7 mm) and number of unit-cells per circumference (3, 7, and 11) on the mechanical response. Results show that increasing the unit-cell count enhances stiffness and Specific Energy Absorption (SEA) but reduces the displacement at which buckling initiates. In contrast, increasing wall thickness simultaneously improves stiffness, peak load, SEA, and instability displacement, with SEA increasing by up to 201% from the thinnest to the thickest configuration. The highest performance was achieved for the 2.7 mm thickness with eleven unit-cells, yielding a peak load of 3679.9 N, stiffness of 4495.2 N/mm, and SEA of 3331.0 mJ/g. The tunable mechanical behavior and lightweight porous architecture position the proposed TPMS metamaterial as a promising candidate for further investigation in load-bearing biomedical applications.

1. Introduction

Mechanical metamaterials represent a paradigm shift in materials science, wherein unusual or extreme mechanical properties arise from designed architectural features at the meso- or microscale rather than from the intrinsic chemical composition of the base material [1–5]. Unlike stochastic foams or conventional porous structures, mechanical metamaterials exhibit rationally designed repeating units that enable precise control over stiffness, strength, energy absorption, and deformation modes [6–9]. Beyond traditional engineering applications, mechanical metamaterials have emerged as promising candidates for biomedical systems due to their ability to provide highly tailorable mechanical and functional properties through architectural design [10,11]. By carefully controlling the internal geometry, these materials can be engineered to achieve desirable combinations of stiffness, strength, energy absorption, permeability, and mass, offering opportunities to address the demanding mechanical and biological requirements of implantable medical devices [12,13]. The design of biomedical implants requires the careful balance of multiple, often competing, mechanical and biological requirements [14,15]. An ideal implant should provide sufficient mechanical strength while maintaining biomechanical compatibility with the surrounding tissue, promoting favorable load transfer, and supporting long-term functional performance [16,17]. Consequently, the development of architected materials capable of tailoring these properties has become an important research direction in modern biomedical engineering [18]. Among the diverse families of

* Corresponding author.
E-mail address: m.fotouhi-1@tudelft.nl (M. Fotouhi).

https://doi.org/10.1016/j.jmrt.2026.08.198
Received 17 June 2026; Received in revised form 13 August 2026; Accepted 22 August 2026
Available online 22 August 2026

mechanical metamaterials (including lattice structures, kirigami/origami-inspired designs, and hierarchical architectures) those based on triply periodic minimal surfaces (TPMS) have attracted particular interest due to their mathematically defined, smooth, non-self-intersecting topologies that approximate ideal minimum-area surfaces [19]. TPMS structures, such as gyroid, diamond, and primitive, offer distinct advantages over strut-based lattices, including reduced stress concentrations, fully interconnected porosity, and high specific surface area [20]. These characteristics make TPMS metamaterials highly promising for applications ranging from lightweight structural components to biomedical implants and energy absorption devices [21].

The gyroid TPMS, in particular, has been extensively studied because it exhibits a unique combination of mechanical efficiency, isotropic behavior, and excellent permeability [22]. Early investigations by Kapfer et al. established the fundamental geometric relationships between sheet- and solid-network gyroid topologies [23]. By means of a finite-element analysis, it was established that the mechanical stiffness of sheet solids was determined to exceed that of conventional network solids over an extensive range of volume fractions and material parameters. Subsequent work by Abueidda et al. demonstrated that gyroid-based structures could achieve stiffness-to-weight ratios comparable to or exceeding those of conventional lattices [24]. More recently, researchers have explored the compressive deformation mechanisms of gyroid TPMS across a range of relative densities. For example, Maskery et al. identified three distinct deformation regimes, namely elastic, plateau, and densification in gyroid structures fabricated via selective laser melting [25]. Similarly, Yang et al. reported that the energy absorption capacity of gyroid lattices could be tailored by adjusting the unit-cell size and wall thickness, with thicker walls promoting a more stable post-yield response [26]. A gyroid structure was theoretically developed based on these findings, which was designed to imitate both the elastic modulus and the compressive strength of human cortical bone. Despite these advances, the majority of existing studies have focused on rectangular or cubic specimen geometries under idealized loading conditions. Cylindrical TPMS configurations are highly relevant for orthopedic and dental implant applications, yet key design parameters, including unit-cell wall thickness and number of unit-cells per circumference remain under-investigated.

In the biomedical domain, the design of load-bearing implants faces persistent challenges related to biomechanical compatibility [27]. Conventional solid metallic implants fabricated from titanium or its alloys exhibit elastic moduli (approximately 110 GPa for Ti–6Al–4V) that are substantially higher than those of human cancellous bone (0.1–2 GPa) and cortical bone (10–30 GPa) [28,29]. This mechanical mismatch leads to the phenomenon of stress shielding, whereby the implant carries a disproportionate share of the physiological load, thereby reducing the mechanical stimulation required for bone remodeling and ultimately promoting bone resorption and implant loosening [30,31]. Porous implant designs have been proposed as a strategy to mitigate stress shielding by reducing the effective stiffness of the implant [32]. However, many porous architectures suffer from compromised fatigue resistance, unpredictable pore interconnectivity, or manufacturing limitations [33]. TPMS-based structures offer an attractive alternative because they combine controlled porosity with mechanical robustness and fully interconnected pore networks that facilitate osseointegration and vascularization [34].

Recent years have witnessed growing interest in applying TPMS metamaterials to biomedical implants [35]. As a case in point, cubic samples of primitive and gyroid structures were designed and prepared by Song et al. with four degrees of porosity for root analogue implant (RAI) [36]. It was found that the yield strengths of these primitive and gyroid structures across all four porosity levels were greater than the yield strength of cortical bone, which was determined to satisfy the requirements for implantation conditions. Additionally, using finite element analysis (FEA), the primitive and gyroid structures with 30% and 40% porosity were shown to exhibit no stress shielding effect. These structures were also proven to promote the growth of surrounding bone tissue and to facilitate long-term and stable osseointegration. By Keshishian and colleagues, three types of RAI dental implants were designed and 3D printed with the aim of overcoming the common limitations of traditional dental implants [37]. These included a solid RAI implant, a gyroid-structured RAI implant, and a functionally graded gyroid-structured RAI implant. Across all three implants, an overall rise in strain energy density was recorded. Notably, the graded implant was found to exhibit a 22% increase in strain energy density, which was interpreted as an indication of its superior biomechanical performance. In a separate investigation, two types of TPMS lattices (gyroid and diamond) were additively manufactured for bone implant purposes [38]. Both lattice types were designed with an interconnected high porosity of 80–95%. Pore sizes were found to range from 560 to 1600 μm for the gyroid structures and from 480 to 1450 μm for the Diamond structures. The porosity of these 80–95% TPMS lattices was observed to be comparable to that of trabecular bone. Additionally, the measured modulus was reported to fall within 0.12–1.25 GPa, making it possible to adjust the lattice modulus to match that of trabecular bone. In the work of Moghariya and Gurrala, two TPMS-based hip implant designs including the gyroid and the Split-P, were modeled following industry standards and were compared against a traditional solid implant [39]. A weight reduction of 28% was calculated for the gyroid-based implant when set against the solid implant, and this design was subsequently concluded to be the most favorable of the three. Furthermore, the gyroid implant was shown to have a porosity of 70% relative to the solid implant, which was considered an important property for osteointegration, thereby supporting bone growth and facilitating tissue regeneration.

In addition to exhibiting adequate static strength, dental implants must withstand millions of cyclic masticatory loading cycles during long-term clinical service. Consequently, fatigue resistance is one of the primary design considerations for load-bearing implant structures. For TPMS-based metamaterials, fatigue performance is strongly influenced by geometric characteristics, including wall thickness, relative density, and stress distribution, as well as by the quality of the additive manufacturing process [40–43]. Therefore, understanding the quasi-static mechanical response and establishing the influence of key geometric parameters on structural behavior constitute essential first steps toward the development of fatigue-resistant TPMS implant architectures. Although the present study focuses on quasi-static compression, the resulting structure–property relationships provide a foundation for future investigations involving cyclic fatigue testing and long-term mechanical reliability of TPMS-based dental implants.

Despite these encouraging results, several critical gaps remain. For example, the majority of TPMS implant studies have employed sheet-based or relatively thick-walled configurations, with limited attention to lightweight, thin-walled cylindrical architectures suitable for dental root analogues. Furthermore, the specific energy absorption (SEA) characteristics of TPMS metamaterials in cylindrical configurations remain poorly understood once the combined effects of wall thickness and number unit-cells per circumference are considered. SEA is a critical metric for applications involving masticatory or impact loads, yet few studies have systematically quantified how geometric parameters influence energy dissipation capacity in gyroid-based cylindrical structures [44]. Beyond demonstrating favorable mechanical performance, TPMS-based implant architectures should also provide practical engineering design guidelines that can support the development of patient-specific implants. In particular, understanding how independent geometric parameters influence stiffness, load-bearing capacity, deformation stability, and energy absorption is essential for rational implant design. Such knowledge enables designers to tailor implant architectures according to specific clinical requirements, including minimizing stress shielding while maintaining sufficient mechanical strength and structural stability. Despite the growing body of research on TPMS structures, relatively few studies have systematically translated the effects of geometric design variables into engineering guidance that can be directly utilized for the optimization of dental implant architectures. Therefore, establishing clear structure–property relationships is not only of scientific interest but also of practical significance for the future design of mechanically optimized additively manufactured dental implants.

The present study addresses these research gaps through a combined experimental and numerical investigation of a thin-walled cylindrical gyroid TPMS architecture intended for potential load-bearing biomedical applications. While cylindrical TPMS structures, gyroid-based implant concepts, and geometric optimization strategies have previously been reported, there remains limited understanding of how the combined variation of wall thickness and circumferential unit-cell number influences the mechanical response of thin-walled cylindrical TPMS architectures. Accordingly, this work first experimentally validates a finite element model using a representative thin-walled cylindrical gyroid specimen and subsequently performs a systematic two-parameter investigation to quantify the influence of these geometric variables on stiffness, peak load, instability onset, and specific energy absorption. By establishing these structure–property relationships, the study provides engineering guidance for the rational design and optimization of future TPMS-based dental implant frameworks and other lightweight load-bearing biomedical structures. It should be noted that although TPMS architectures have demonstrated considerable potential for biomedical applications, their translation into clinically applicable dental implants requires comprehensive multidisciplinary evaluation beyond quasi-static mechanical characterization. In addition to mechanical performance, implant-level finite element analyses under physiological loading conditions, stress-shielding assessment, fatigue behavior under cyclic mastication, osseointegration, biocompatibility, and comparisons with established commercial implant designs are essential for clinical validation. Consequently, the present work should be regarded as a foundational mechanical investigation of a thin-walled cylindrical gyroid TPMS architecture intended to establish structure–property relationships and provide engineering insight for future implant development. The mechanical understanding developed herein provides the basis for subsequent implant-specific analyses and biological evaluations required for clinical translation.

2. Materials and methods

2.1. Design of the gyroid-based TPMS architecture

The cylindrical metamaterial investigated in this study was generated using a triply periodic minimal surface (TPMS) of the gyroid type. The gyroid surface was mathematically defined by the implicit equation:

$$\sin\left(\frac{2\pi x}{L}\right)\times\cos\left(\frac{2\pi y}{L}\right)+\sin\left(\frac{2\pi y}{L}\right)\times\cos\left(\frac{2\pi z}{L}\right)+\sin\left(\frac{2\pi z}{L}\right)\times\cos\left(\frac{2\pi x}{L}\right)=C$$

where L represents the unit-cell length and C is a level-set constant controlling the volumetric offset. By varying C, the wall thickness of the TPMS network could be systematically adjusted while preserving the overall topology. The cylindrical specimen geometry was obtained by wrapping the gyroid unit cells around a central axis, creating a tubular structure with a fixed outer diameter and height. Two independent design parameters were selected for parametric investigation: (i) the wall thickness of the gyroid network (1.1 mm, 1.9 mm, and 2.7 mm), and (ii) the number of unit-cells arranged around one full circumference (3, 7, and 11). All other geometric attributes (including overall cylinder height, outer diameter, and the axial length of the specimen) were held constant across all configurations.

2.2. Raw material and physical properties

Specimens were additively manufactured using resione k + selected for its capacity to produce lattices with fine features showing no brittle failure under compression. The resin exhibited an elastic modulus of 1180 MPa and a Poisson's ratio of 0.3 under dry, room-temperature conditions, as reported by the supplier. However, to account for the influence of the printing process on effective mechanical properties (particularly the anisotropic behavior introduced by layer-wise fabrication and the effect of post-curing on network stiffness) an inverse calibration procedure was performed. A representative specimen (thickness = 1.9 mm, eleven unit-cells per circumference) was fabricated, compression-tested, and its initial elastic response was used to refine the Young's modulus in the finite element model (Fig. 2). The calibration iteratively adjusted the modulus until the simulated force–displacement slope matched the experimental measurement within a 3% tolerance. The calibrated modulus value was then applied uniformly across all subsequent parametric simulations. The mass density of the printed resin was determined by measuring the mass of three as-printed specimens of known volume using a precision balance (accuracy ±0.0001 g), yielding an average value of 0.0011 g/mm^3, which was subsequently used for specific energy absorption normalization.

2.3. Additive fabrication workflow

All physical test samples were produced using a digital light processing (DLP) 3D printer. The printing orientation was selected such that the longitudinal axis of the cylindrical specimen aligned vertically with the build platform, minimizing support structure requirements and reducing surface roughness on the load-bearing faces. The layer thickness was set to 50 μm, and exposure parameters were optimized for the chosen resin to ensure complete polymerization of thin TPMS walls without over-curing that could close small pores. After printing, each specimen was removed from the build platform and rinsed in a 99% isopropyl alcohol bath for 8 min under ultrasonic agitation to dissolve residual uncured resin from the internal gyroid channels. Following rinsing, specimens were dried using compressed air and subsequently post-cured in a UV oven for 25 min to maximize cross-linking density and stabilize mechanical behavior. No additional surface coating, heat treatment, or infiltration was applied. Each specimen was inspected under a digital microscope to verify the absence of occluded resin pockets, incomplete wall formation, or delamination between layers. Specimens exhibiting visible defects were excluded from further testing.

2.4. Quasi-static compression testing

Compression experiments were performed using a universal testing machine fitted with a 10 kN load cell and two hardened steel compression plates. The lower plate was fixed, while the upper plate was actuated in displacement control mode. Each cylindrical specimen was positioned centrally on the lower platen, and the upper platen was lowered until a preload of approximately 2 N was registered to ensure full contact without initial indentation. A constant crosshead speed of 0.5 mm/min was applied to maintain quasi-static conditions throughout the test, given the relatively stiff TPMS architecture. Data acquisition was performed at a sampling rate of 50 Hz, recording force, displacement, and time continuously. Compression was continued until the specimen reached 60% of its original height or until a clear post-peak softening plateau was established. To assess repeatability, five nominally identical specimens were tested for the reference configuration (1.9 mm thickness, eleven unit-cells per circumference). The initial stiffness was calculated by linear regression of the force–displacement data over the interval from 0 mm to 0.5 mm of displacement, ensuring that the analysis captured only the elastic regime. Specific energy absorption (SEA) was obtained by trapezoidal numerical integration of the force–displacement curve from zero to the final displacement, followed by division by the specimen's mass.

2.5. Finite element simulation setup

Numerical simulations were conducted using Abaqus/Explicit (Dassault Systèmes, version 2022). The CAD geometry of each specimen was imported as a solid body and meshed using linear tetrahedral mesh elements (C3D4) to better capture the curvature of the gyroid surface compared to linear elements. The material was modeled using an isotropic elastic–plastic constitutive formulation. Elastic behavior was defined using the calibrated Young's modulus and Poisson's ratio, while plastic deformation was described using the experimentally calibrated stress–strain relationship. Yielding was assumed to follow the von Mises yield criterion with isotropic hardening. The TPMS specimens were discretized using four-node linear tetrahedral elements (C3D4). Following the mesh convergence study described, an average element size of 1 mm was selected, resulting in approximately 2,005,456 elements for the reference model. The selected mesh provided a suitable balance between computational efficiency and numerical accuracy, see Fig. 1b. The explicit dynamic formulation was selected despite the quasi-static nature of the physical experiments because of its superior convergence behavior in problems involving complex contact, large deformations, and post-buckling response, all of which were expected in the gyroid TPMS architecture under compression. The kinetic energy remained below 2% of the internal energy throughout the simulations, confirming quasi-static loading conditions.

2.6. Loading and boundary replication

The boundary conditions were defined to mimic the experimental compression setup as faithfully as possible. The bottom surface of the cylindrical specimen was fully constrained in all translational degrees of freedom ($Ux = Uy = Uz = 0$), representing the fixed lower plate. The upper plate was modeled as a discrete rigid body with a reference node at its center. A displacement-controlled boundary condition was applied to the reference node, moving the rigid plate vertically downward at a

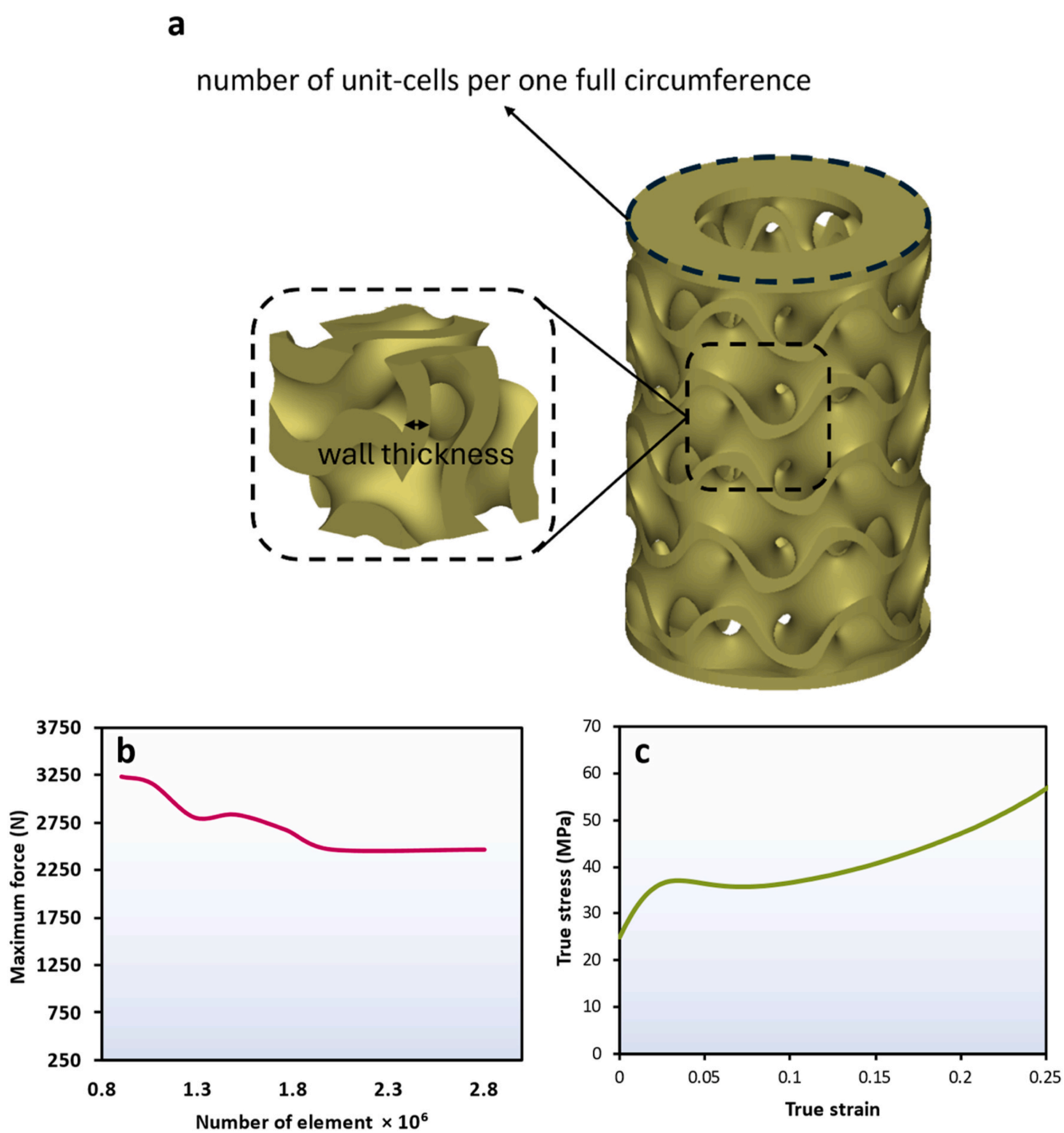

Fig. 1. a) Design parameters for parametric investigation, b) mesh convergence analysis, and c) calibrated plastic stress–strain relationship.

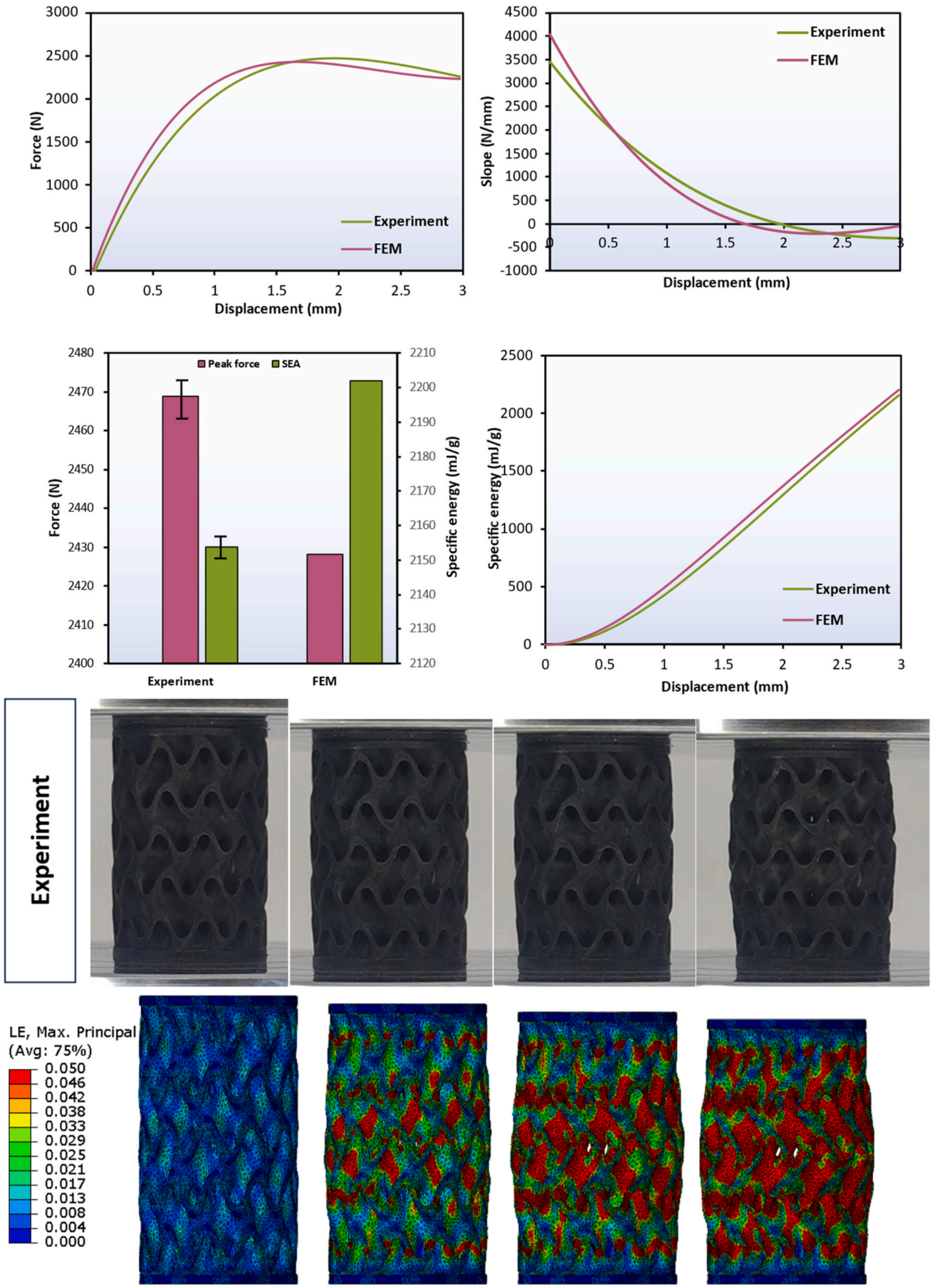

Fig. 2. Experimental validation of FEM predictions for the 1.9-mm-thick cylindrical metamaterial, where eleven unit-cells complete one round of the circumference.

constant velocity of 0.5 mm/min, identical to the experimental cross-head speed. Contact between the specimen and both plates was modeled using a penalty friction formulation with a coefficient of friction of 0.05. Additionally, general contact (self-contact) was activated to capture interactions between adjacent gyroid walls as the structure deformed and buckled. The normal contact behavior was defined as hard contact, allowing separation but preventing interpenetration. The total simulation duration was set to 15 s, sufficient to capture the full elastic regime, peak load, and post-peak softening. The ratio of kinetic energy to internal energy was monitored throughout each simulation; this ratio remained below 5% for all configurations, confirming that inertial effects were negligible and that the explicit simulations effectively reproduced quasi-static conditions.

2.7. Validation protocol

The fidelity of the finite element model was assessed by comparing its predictions against experimental measurements for the reference configuration (1.9 mm thickness, eleven unit-cells per circumference). Three quantitative metrics were employed: (i) the coefficient of determination (R^2) between the simulated and experimental force–displacement curves across the entire compression range, (ii) the relative error in peak load, and (iii) the relative error in SEA at the final displacement. Qualitative validation was also performed by comparing experimentally photographed deformation sequences at 10%, 30%, 50%, and 70% compression with simulated von Mises stress contour plots at equivalent displacement increments. The model was considered validated if R^2 exceeded 0.95, peak load error remained below 5%, and the deformation sequences showed visual correspondence. Following calibration and validation against the reference configuration, the calibrated constitutive model was kept unchanged and applied to all remaining geometric configurations without further parameter adjustment. Accordingly, the simulations of the remaining configurations represent model-based predictions of the geometric effects rather than independently experimentally validated results. It should be noted that, the average experimental force–displacement response of the five reference specimens was used for inverse calibration of the effective constitutive response of the printed material. The Young's modulus was calibrated from the initial elastic region, while the plastic constitutive response was obtained by calibrating the corresponding stress–strain relationship (Fig. 1b) against the experimentally observed nonlinear response. The calibrated constitutive parameters were then fixed and used without further adjustment in all subsequent simulations. It should be noted that, the corresponding Young's modulus and Poison ration derived from calibration was 1180 MPa, and 0.3, respectively.

3. Results and discussion

3.1. Validation of the finite element model against experimental measurements

To ensure the reliability of the subsequent numerical parametric study, the finite element (FE) model was first validated against physical experiments. A cylindrical metamaterial specimen based on the proposed novel TPMS architecture was fabricated via 3D printing. The selected test sample featured a wall thickness of 1.9 mm and consisted of eleven unit-cells arranged contiguously along one full circumference. Quasi-static uniaxial compression tests were conducted on the 3D-printed specimen, with the experiment repeated five times to account for any variability in the fabrication or testing procedure; the reported experimental data represent the averaged mechanical response. An identical model was then simulated using Abaqus/Explicit under equivalent loading and boundary conditions, as shown in Fig. 2. Beyond quantitative force–displacement comparison, particular attention was given to the deformation behavior of the TPMS structure throughout the compression process. Both the numerical predictions and experimental observations captured a consistent sequence. Quantitative comparison between the simulated and experimental force–displacement curves yielded a coefficient of determination of $R^2 = 0.965$, indicating excellent agreement. The close agreement between the simulated and experimentally measured responses both in terms of force–displacement curves and morphological evolution, confirms the validity of the FE modeling approach. This validation provides a solid foundation for the subsequent analysis of parameter effects and design optimization presented in the following subsections. Examination of the force–displacement response obtained from compressive deformation of the novel TPMS structure (presented in Fig. 2) reveals two distinct deformation phases. Accordingly, at the initial stage of deformation, the compressive force increases sharply until a displacement of approximately 0.75 mm is reached, which corresponds to 25% deformation. Examination of the corresponding strain contour plots reveals that the structure experiences no considerable strain accumulation during this phase. Furthermore, the strain contour indicates that the response remains mainly within the elastic regime. This initial steep rise in force is attributed to the inherent stiffness of the TPMS architecture, where the interconnected unit cells collectively resist the applied load without undergoing permanent morphological changes. This elastic behavior persists until the critical displacement threshold is exceeded, after which the structure transitions into the second deformation phase. Afterward, it can be seen that phase two is more complicated than the first phase. Initially, the force increases with a decreasing stiffness until it reaches its peak at around 1.6 mm displacement. At this peak, the experimental measurement recorded a maximum compressive load of 2468.8 N, while the finite element simulation yielded a closely corresponding value of 2428.3 N, as indicated in Fig. 2. The slight difference of approximately 1.6% between the two values further corroborates the validity of the numerical model. Following this peak, the force–displacement curve shows that the force decreases with a slight slope until the end of compression deformation. Regarding the strain evolution, it can be observed that after 25% deformation, elements gradually undergo plastic deformation. Plasticity first initiates at the core of the novel TPMS structure between two neighboring gyroid unit-cells. From this localized region, plastic deformation subsequently develops further and results in global buckling of the novel TPMS structure through the deflection of the unit-cells located at the core. Further deformation until the end of the compression process only leads to more pronounced buckling, with no additional failure modes emerging. This two-phase deformation behavior, characterized by an initial elastic regime followed by plasticity-driven buckling, demonstrates the unique mechanical response of the proposed TPMS metamaterial. In other words, at this stage, high-strain regions initiated within the ligaments connecting adjacent engineered voids of the TPMS unit cells. As compression progressed, these localized deformation regions propagated through the structure, producing a barrel-shaped global deformation mode centered within the specimen.

In addition to force–displacement behavior, the specific energy absorption (SEA) of the novel TPMS metamaterial was evaluated to further assess its energy dissipation capability. The SEA, defined as the total absorbed energy per unit mass of the structure, was calculated by integrating the area under the force–displacement curve and normalizing by the specimen's mass. Fig. 2 presents the SEA–displacement curves obtained from both the finite element simulation and experimental measurements. The two curves exhibit excellent agreement throughout the entire compression process, further reinforcing the validity of the numerical model. It should be noted that previous investigations have suggested that the absence of fluctuations during the ascending portion of the SEA–displacement curve indicates stable energy absorption behavior throughout compression [45,46]. At the end of the deformation, the FEM predicted a final SEA value of 2202 mJ/g, while the experimental measurement yielded 2153.8 mJ/g. The close correspondence between these values, with a relative difference of approximately 2.2%, demonstrates that the proposed TPMS architecture offers a highly competitive energy absorption capacity. Although additive manufacturing inevitably introduces minor geometric deviations and surface irregularities, the close agreement between the experimental and numerical results ($R^2 = 0.965$) indicates that these imperfections had a negligible influence on the global compressive behavior investigated in the present study. Although the finite element model assumes an idealized CAD geometry and homogeneous material properties, the additively manufactured specimens may contain minor geometric deviations and surface imperfections resulting from the layer-by-layer fabrication and post-processing procedures. Such deviations may include small variations in TPMS wall thickness, local surface irregularities, and dimensional differences from the nominal CAD geometry. These imperfections can locally modify the load-transfer paths and stress distribution within the TPMS network and may therefore contribute to the differences observed between the experimental and numerical force–displacement responses. In particular, local deviations in the thickness or curvature of the TPMS walls can influence the initiation and propagation of strain localization during compression.

3.2. Geometric parametric analysis

To explore the design space of the proposed cylindrical TPMS metamaterial, this section examines the effect of two primary geometric parameters: wall thickness and the number of unit-cells arranged around the circumference. Both parameters play a fundamental role in defining the relative density and, consequently, the mechanical response of the structure. Building upon the validated FE model, a series of simulations was performed across a range of thicknesses and unit-cell counts. The force–displacement curves, deformation sequences, and SEA values obtained from these parametric runs are systematically analyzed. The findings reveal clear trends that enable the tuning of mechanical performance for target engineering applications. A total of nine finite element simulations were conducted, covering all combinations of three thickness values (1.1 mm, 1.9 mm, and 2.7 mm) and three unit-cell counts (three, seven, and eleven per circumference). The complete set of results, including peak load, initial stiffness, specific energy absorption, and instability displacement, is summarized in Table 1. It should be noted that, the instability point was defined as the displacement corresponding to the first negative slope in the force–displacement curve, indicating the onset of global structural instability.

In this regard, Fig. 3 illustrates the influence of number of unit-cells arranged around one full circumference on mechanical response of the cylindrical TPMS metamaterial. As demonstrated in Fig. 3a, while the two distinct phases discussed earlier are present across all force–displacement curves irrespective of the unit-cell count, this geometric parameter nevertheless exerts a considerable influence on the behavior observed within each phase. With respect to Phase 1, a clear trend can be observed from Fig. 3a, b, and 3d, in which a higher number of unit-cells leads to a substantial enhancement in the structural stiffness of the proposed TPMS metamaterial. Fig. 3d shows that, the stiffness related to TPMS structure with three, seven and eleven unit-cells per one circle is 499.9 N/mm, 1231.9 N/mm, and 1697.4 N/mm, respectively. This stiffness enhancement can be attributed to the geometric reorganization imposed by changing the number of unit-cells around the fixed circumference. Although the overall cylindrical envelope remains unchanged, reducing the number of unit-cells per circumference results in a larger void space within each individual gyroid unit-cell. Conversely, increasing the unit-cell count divides the same circumferential length into a greater number of smaller, more compact unit-cells. Under compressive loading, the strain distribution across the structure remains qualitatively similar regardless of unit-cell number (Fig. 4). However, the presence of larger voids in configurations with fewer unit-cells (e.g., three unit-cells per circle) creates wider unsupported regions within the TPMS architecture. These larger voids are more susceptible to local deformation under the same applied load, effectively reducing the overall structural stiffness. In contrast, configurations with a higher number of unit-cells (e.g., eleven unit-cells per circle) feature smaller, more frequently interconnected voids, which distribute the applied load more evenly throughout the structure and provide additional load-bearing pathways. This refined network of smaller unit-cells resists elastic deformation more effectively, thereby yielding the observed increase in initial stiffness. The same trend has been reported via Laskowska et al. [47]. They reported that for bending-dominated structures, increasing the number of cells per round yields similar yield strength but significantly higher plateau stress compared to stretch-dominated counterparts. While the absolute stiffness values discussed above reflect the structural response of each configuration, they do not distinguish between gains arising from increased material content versus those arising from more efficient load distribution. To isolate the role of topology, the specific stiffness, defined as stiffness normalized by specimen mass, is shown in Table 1. For configurations with three, seven, and eleven unit-cells per circumference (at a constant wall thickness of 1.1 mm), the specific stiffness values are 184.94 N mm/g, 379.01 N mm/g, and 470.02 N mm/g, respectively. this improvement arises purely from geometric reorganization: subdividing the same circumference into a greater number of smaller, more interconnected unit-cells creates additional load paths and distributes stress more evenly, enabling each gram of material to contribute more effectively to load bearing. In other words, the higher specific stiffness of the eleven-cell configuration is a direct consequence of topological efficiency, not material quantity.

The proposed cylindrical TPMS metamaterial, as evidenced by the smooth rising stage without oscillations and the stable plateau region in Fig. 3a, exhibits behavior characteristic of bending-dominated structures [48,49]. Consistent with Laskowska et al. [47] findings, our results show that a higher unit-cell count (from three to eleven) enhances stiffness and peak load.

Regarding the second deformation phase, the peak load magnitude clearly scales with the number of unit-cells. As reported in Fig. 3c, the peak load reaches 459 N for three unit-cells, 997 N for seven unit-cells, and 1310 N for eleven unit-cells. This direct correlation between peak load and unit-cell count stems from the same geometric mechanism responsible for the stiffness enhancement in Phase 1. Configurations with fewer unit-cells contain larger gyroid void spaces, which not only reduce elastic stiffness but also create regions of geometric weakness where plastic deformation initiates more readily under continued loading. Once plastic yielding begins at the core between neighboring

Table 1
Summary of parametric simulation results for the cylindrical TPMS metamaterial under compressive loading.

Gyroid Thickness (mm)	Number of unit-cell per circle	Peak load (N)	Specific stiffness (N/g.mm)	SEA (mJ/g)	Instability displacement (mm)	Relative density (%)
1.1	3	454.9	184.94	403.5	1.73	5.78
1.1	7	997	379.01	902.4	1.64	6.95
1.1	11	1310	470.02	1179.3	1.52	7.72
1.9	3	867.9	237.49	772.9	1.92	8.36
1.9	7	1863.1	456.22	1687	1.81	10.39
1.9	11	2428.3	552.20	2202	1.66	11.73
2.7	3	1380.9	278.45	1215.6	2.16	10.94
2.7	7	2833.8	508.2	2552.9	1.91	13.85
2.7	11	3679.9	610.25	3331	1.74	15.76

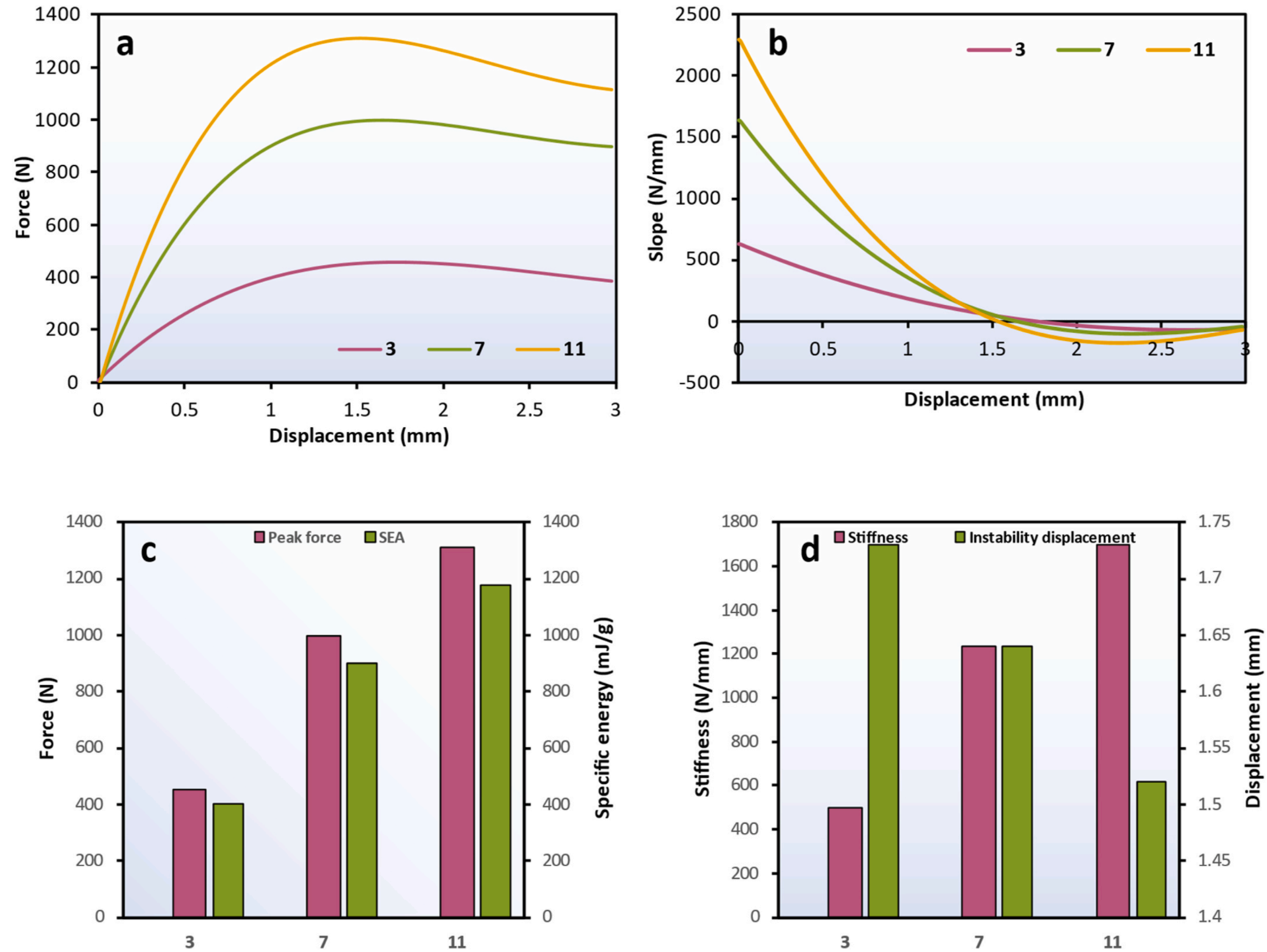

Fig. 3. Mechanical response of the cylindrical TPMS metamaterial as a function of the number of unit-cells arranged around one full circumference, with the wall thickness maintained at 1.1 mm: (a) full force–displacement curves, (b) corresponding stiffness–displacement evolution, (c) extracted peak load and end-of-deformation SEA values, and (d) the initial stiffness alongside the displacement threshold marking the onset of structural instability.

unit-cells, the larger voids in low unit-cell-count structures provide less resistance against the propagation of buckling (Fig. 4). Consequently, the structure reaches its load-bearing capacity at a lower peak force. In contrast, increasing the number of unit-cells produces a denser network of smaller, interconnected cells. This refined architecture offers more numerous load paths and better confinement of plastic deformation, allowing the structure to sustain substantially higher compressive forces before peak load is attained. The progressive increase from 459 N to 1310 N as the unit-cell count rises from three to eleven thus reflects a transition from a void-dominated, weak architecture to a highly interconnected, load-resilient metamaterial. However, this enhancement in stiffness and peak load comes with a trade-off regarding the onset of structural instability. Although a higher number of unit-cells significantly improves the load-bearing capacity, it accelerates the initiation of buckling. As shown in Fig. 3d, the displacement at which instability begins decreases as the unit-cell count increases: 1.73 mm for three unit-cells, 1.64 mm for seven unit-cells, and 1.52 mm for eleven unit-cells. This earlier onset of buckling can be explained by the increased structural complexity and interconnectivity of the TPMS network. In other words, increasing the number of unit-cells was associated with a delayed onset of global structural instability. With more unit-cells packed into the same circumferential length, the walls become more densely arranged and experience higher localized stresses at smaller deformations (Fig. 4). The refined network, while stiffer, also transmits loads more rapidly to critical junctions between neighboring unit-cells, triggering plastic instability sooner. In other words, the very geometric refinement that enhances stiffness and peak load also reduces the structure's ability to delay buckling, indicating a design trade-off between load capacity and deformation range. It is important to highlight that the specific energy absorption is also strongly and positively influenced by the number of unit-cells, with measured values of 403.5 mJ/g, 902.4 mJ/g, and 1179.3 mJ/g for configurations containing three, seven, and eleven unit-cells per circumference, as shown in Fig. 3c.

Further insight into the underlying deformation mechanisms can be gained by examining the evolution of plastic deformation, quantified here as the fraction of soft modes (i.e., the proportion of elements that have undergone yielding) throughout the compression process, as presented in Fig. 5. Several important observations emerge from this analysis. First, the activation of plastic deformation occurs at different displacement thresholds depending on the unit-cell count. For configurations with three and seven unit-cells per circumference, plasticity initiates at approximately 0.23 mm. In contrast, the structure with eleven unit-cells exhibits earlier plastic activation, beginning at around 0.11 mm. This earlier onset is consistent with the previously noted trade-off: the denser, more interconnected network of smaller unit-cells generates higher localized stresses at smaller deformations, triggering yielding sooner despite the overall stiffness enhancement.

Second, across all displacement levels, the fraction of soft modes is

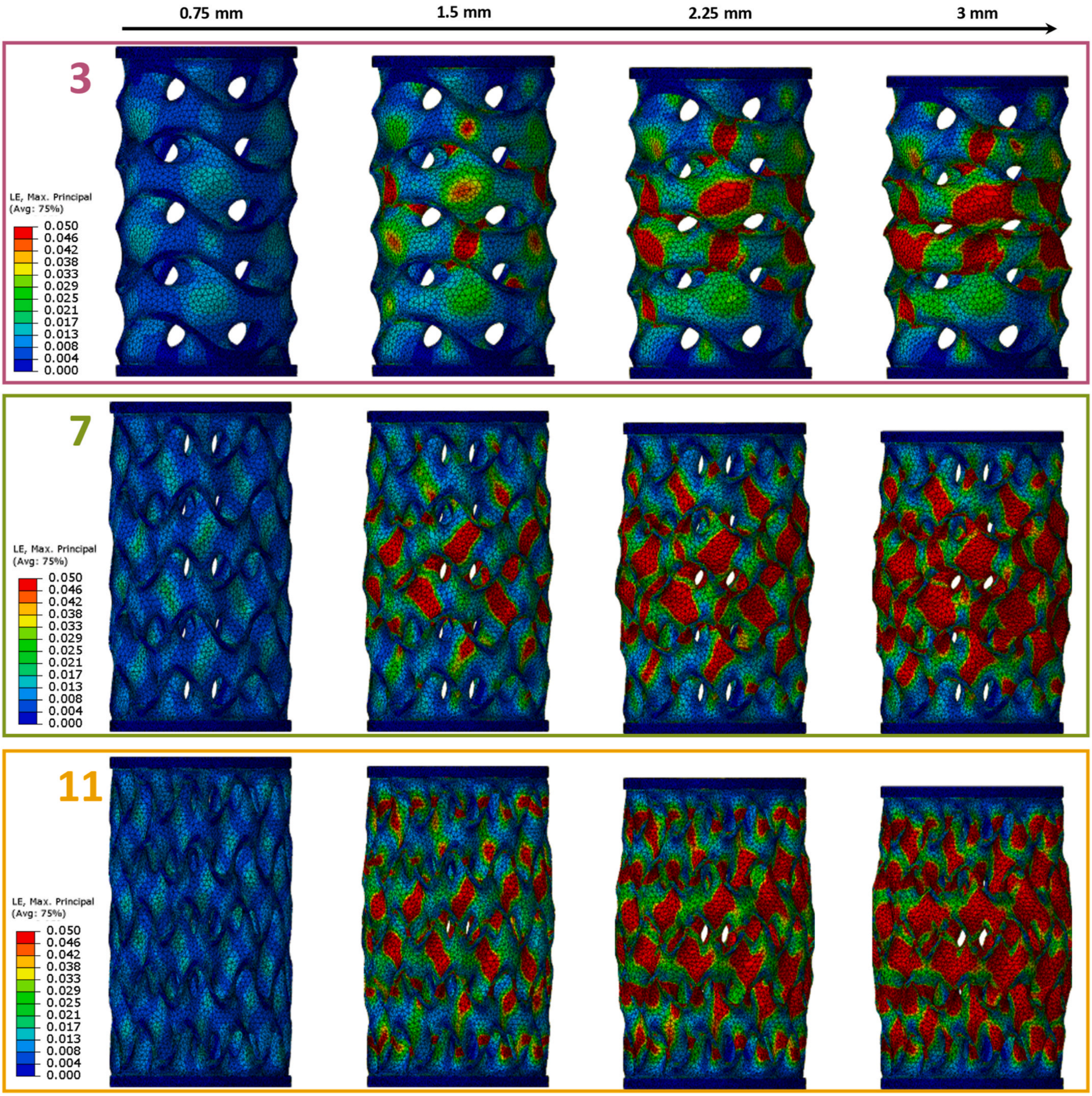

Fig. 4. Influence of number of unit-cells arranged around one full circumference with the wall thickness maintained at 1.1 mm on the distribution of strain during deformation.

consistently greater for structures with a higher number of unit-cells. At the end of deformation, the soft mode fraction reaches 7% for three unit-cells, 13.3% for seven unit-cells, and 18.5% for eleven unit-cells. This trend directly correlates with the earlier observation that higher unit-cell counts produce greater peak loads and SEA values. A larger fraction of yielded elements indicates that more of the structure has been mobilized to dissipate energy through plastic work, rather than remaining elastically unloaded. In the three-unit-cell configuration, the larger void spaces create wide unsupported regions where deformation localizes into a narrow band, leaving substantial portions of the structure minimally deformed. Conversely, the eleven-unit-cell architecture distributes plasticity across a much larger proportion of the TPMS network, as the smaller, more interconnected cells force the deformation to propagate through multiple load paths. This more widespread plastic activity explains the substantially higher energy absorption (1179.3 mJ/g vs. 403.5 mJ/g) despite the earlier onset of instability. In summary, increasing the number of unit-cells transforms the deformation mode from a localized, low-plasticity response to a distributed, high-plasticity mechanism, which enhances load capacity and energy absorption at the expense of earlier plastic activation and buckling initiation.

Having established the influence of the number of unit-cells around the circumference, this subsection examines the second key geometric parameter: the wall thickness of the TPMS unit-cell. Thickness directly governs the relative density of the metamaterial and, consequently, its resistance to deformation, load-bearing capacity, and energy absorption efficiency. Using the validated FE model, a series of simulations was

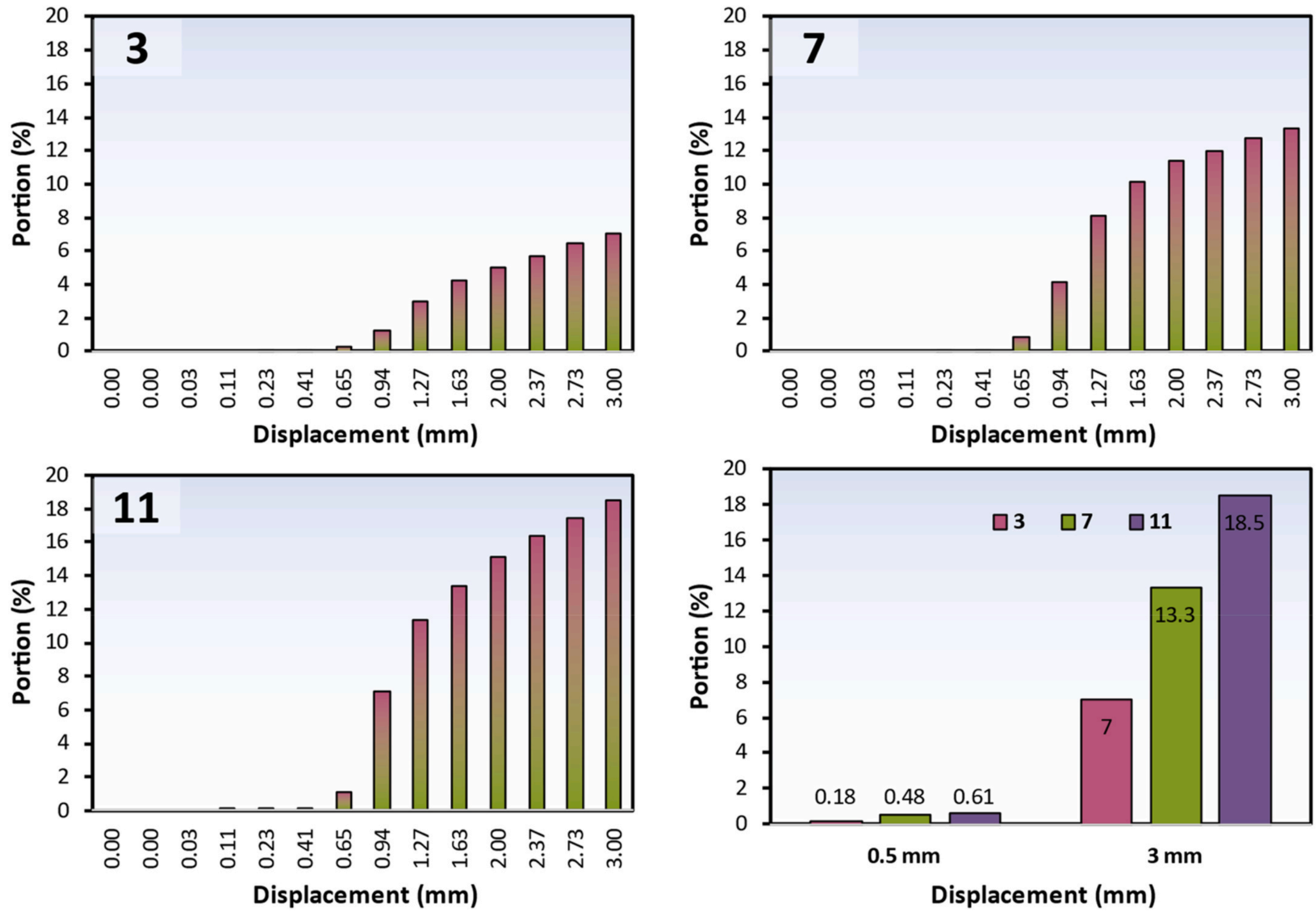

Fig. 5. Influence of number of unit-cells arranged around one full circumference with the wall thickness maintained at 1.1 mm on evolution of plastic deformation.

performed across a range of thickness values while keeping the number of unit-cells fixed at three per circumference. The thickness values investigated, the resulting force–displacement responses, stiffness evolution, peak loads, SEA values, and instability onset displacements are systematically presented and discussed below. In this context, Fig. 6 is provided, which shows the effect of Gyroid thickness on the mechanical performance of the novel TPMS structure. As illustrated in Fig. 6a, analogous to the effect of unit-cell count, varying the unit-cell thickness does not alter the occurrence of the two previously identified phases in the force–displacement response; however, certain characteristics within each phase are modified. As a clear illustration, increasing the unit-cell thickness proportionally enhances the structural stiffness, in which values of 449.9 N/mm, 927.9 N/mm, and 1424.4 N/mm are obtained for thicknesses of 1.1 mm, 1.9 mm, and 2.7 mm, respectively (Fig. 6b and d). This positive correlation between thickness and stiffness is attributed to the increased cross-sectional area of the TPMS network.

While the absolute stiffness values increase with wall thickness, this trend is partially expected because thicker walls introduce more solid material into the structure. The observed increase in stiffness with wall thickness can be attributed to the larger effective load-bearing cross-sectional area of the gyroid network. Thicker TPMS ligaments possess higher bending rigidity and are therefore more resistant to elastic deformation under compressive loading. Consequently, the applied load is distributed more uniformly throughout the interconnected network, reducing localized deformation and increasing the overall structural stiffness. To decouple the effect of material quantity from that of topological efficiency, the specific stiffness normalized by specimen mass presented in Table 1. For thicknesses of 1.1 mm, 1.9 mm, and 2.7 mm (with the number of unit-cells fixed at three per circumference), the specific stiffness values are 184.94 N mm/g, 237.49 N mm/g, and 278.45 N mm/g, respectively. The rising trend in specific stiffness demonstrates that the thicker-walled TPMS network distributes loads more efficiently across its cross-section, activating a larger fraction of the material to resist deformation before the onset of yielding. In other words, increasing wall thickness not only adds material but also enhances the topological efficiency of the gyroid architecture, as the thicker walls provide greater bending and stretching resistance at critical load-bearing junctions.

As the wall thickness grows, more solid material is distributed throughout the gyroid architecture, enhancing the local bending and stretching resistance of each individual strut-like element. Consequently, the structure requires a higher applied force to achieve the same level of elastic deformation. The stiffness–displacement curves (presented in Fig. 6b) further reinforce this trend, showing that throughout the entirety of first phase, configurations with greater thickness consistently exhibit higher instantaneous stiffness compared to their thinner counterparts. In other words, from the onset of compression until the transition to Phase 2, the 2.7 mm thick specimen maintains a stiffness advantage over the 1.9 mm specimen, which in turn outperforms the 1.1 mm configuration at every displacement increment. Therefore, it is reasonable to conclude that increasing the Gyroid thickness will results in enhancement of peak force, which is showed in Fig. 4d. Furthermore, the increased cross-sectional area of the TPMS network delays the onset of local yielding and distributes deformation

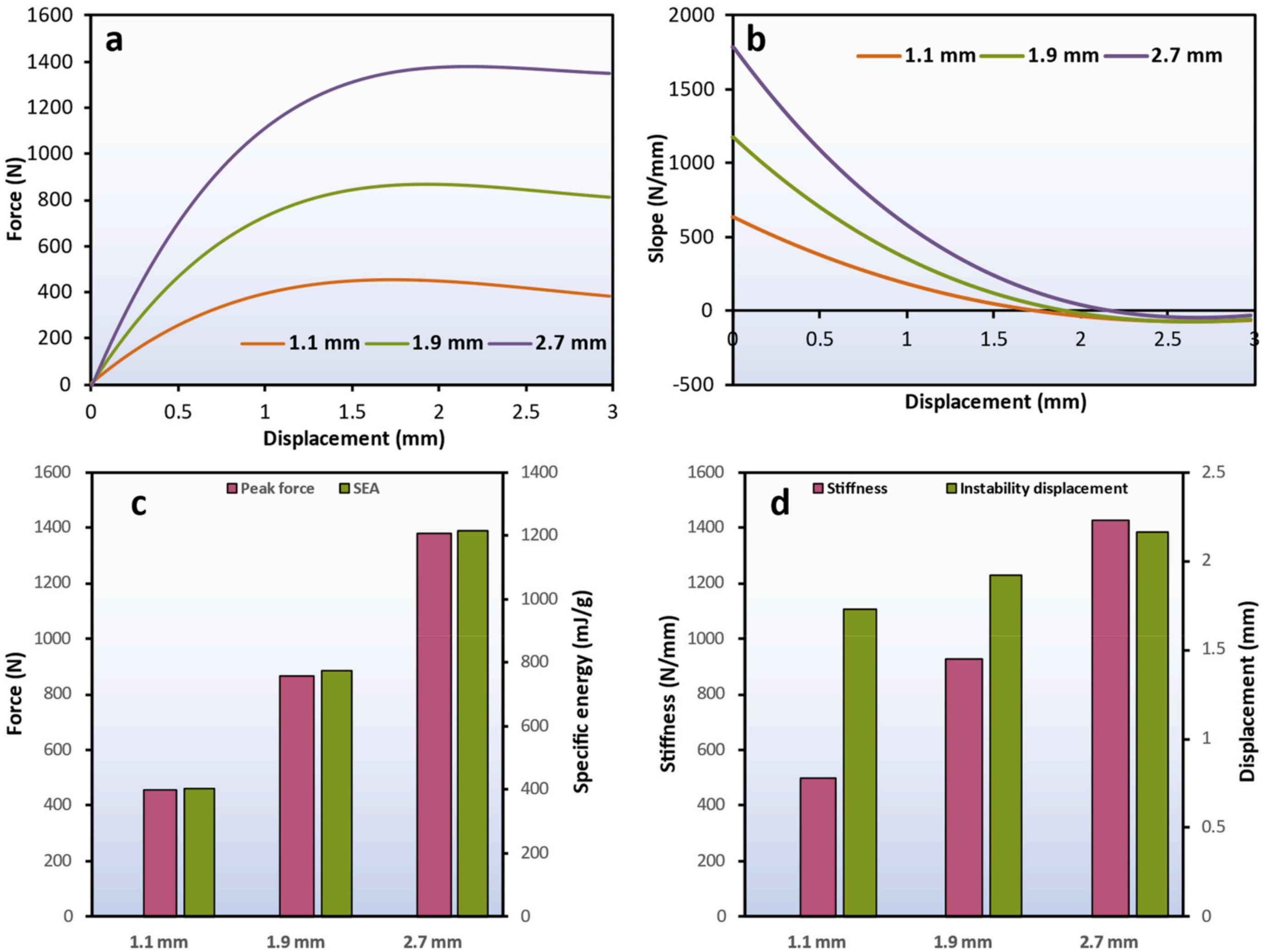

Fig. 6. Mechanical response of the cylindrical TPMS metamaterial as a function of the unit-cell thickness, with the number of unit-cells arranged around one full circumference maintained at 3: (a) full force–displacement curves, (b) corresponding stiffness–displacement evolution, (c) extracted peak load and end-of-deformation SEA values, and (d) the initial stiffness alongside the displacement threshold marking the onset of structural instability.

more effectively (Fig. 7), allowing the structure to sustain substantially higher forces. This delay in local yielding also positively influences the onset of global structural instability. As the wall thickness increases, the displacement at which buckling initiates shifts to larger deformation levels. Specifically, for the specimen with a thickness of 1.1 mm, instability begins at a displacement of 1.73 mm. Increasing the thickness to 1.9 mm raises this threshold to 1.92 mm, and a further increase to 2.7 mm pushes the instability onset further to 2.16 mm. This progressive enhancement occurs because thicker walls provide greater bending resistance at the critical junctions between neighboring gyroid unit-cells, where plastic deformation typically first emerges. The augmented cross-section requires more extensive yielding before local instabilities can coalesce into global buckling. In other words, the improvement in peak load is associated with the enhanced load-bearing capacity of the interconnected TPMS network. Increasing the wall thickness increases the cross-sectional area available to resist compressive stresses, while a larger number of unit-cells promotes a more homogeneous stress distribution throughout the structure. As a result, stress concentrations within individual ligaments are reduced, delaying the onset of structural instability and allowing the framework to sustain higher compressive loads before failure. Consequently, unlike the trade-off observed with increasing unit-cell count (where denser packing accelerated instability), thickening the TPMS network simultaneously improves load capacity, and deformation stability, making it a more straightforward and universally beneficial design strategy for applications requiring robust mechanical performance across an extended compression range.

Beyond enhancing buckling resistance and load-bearing capacity, unit-cell thickness also exerts a substantial influence on the specific energy absorption of the novel TPMS metamaterial, as presented in Fig. 6c. Inspection of this figure reveals that increasing the thickness from 1.1 mm to 1.9 mm yields an SEA improvement of nearly 91%, while a further increase to 2.7 mm produces an increase of approximately 201% relative to the thinnest configuration. This substantial SEA enhancement stems from two synergistic mechanisms. First, as established earlier, thicker walls generate significantly higher force levels throughout the entire compression process, from the elastic regime through post-buckling deformation. Since SEA is calculated as the integrated area under the force–displacement curve normalized by mass, the elevated force response directly translates into greater energy absorption per unit mass. Second, unlike the trade-off observed with increasing unit-cell count, thicker specimens also sustain deformation over a longer displacement range before instability initiates (increasing from 1.73 mm to 2.16 mm). This extended deformation window allows the structure to absorb additional energy even after yielding begins. The combination of higher forces and prolonged deformation range produces the marked 201% SEA improvement observed when moving from the thinnest (1.1 mm) to the thickest (2.7 mm) configuration. Notably,

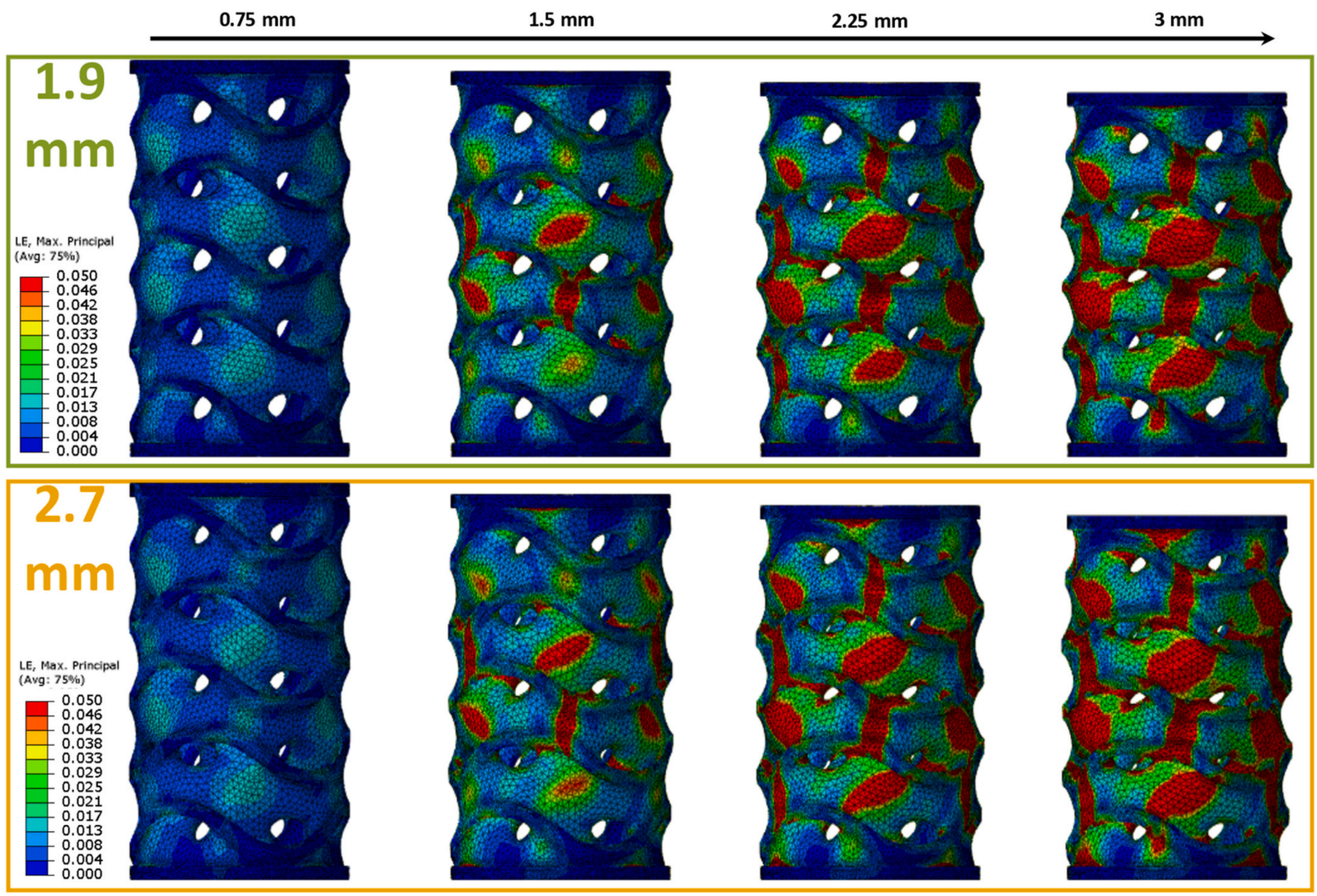

Fig. 7. Influence of unit-cell thickness for TPMS structure with constant three unit-cells arranged around one full circumference on the distribution of strain during deformation.

this enhancement is achieved without the penalty of earlier buckling, confirming that thickness adjustment is a particularly effective and straightforward design parameter for maximizing the energy absorption performance of the proposed gyroid-based cylindrical metamaterial.

Further mechanistic insight into thickness-dependent behavior is provided by analyzing the evolution of plastic deformation, quantified as the fraction of soft modes (proportion of yielded elements) throughout compression, as shown in Fig. 8. Unlike the trend observed with unit-cell count, where higher cell numbers accelerated plastic activation, increasing wall thickness delays the onset of yielding. Plastic deformation activates at approximately 0.11 mm for the 1.9 mm thick specimen, whereas for the 2.7 mm thickness, activation shifts to a later displacement of 0.23 mm. This delay occurs because thicker walls require a larger accumulated strain before local stresses reach the yield threshold at critical junctions between neighboring gyroid unit-cells. Furthermore, once yielding begins, the fraction of soft modes at any given displacement is consistently greater for thicker structures. At the end of deformation, the soft mode fraction reaches 7% for the 1.1 mm thickness, 11.1% for the 1.9 mm thickness, and 15.6% for the 2.7 mm thickness. This combination, i.e. later activation but ultimately higher final soft mode fraction, reveals an important mechanistic distinction from the unit-cell count effect. Thicker walls not only resist the initiation of plasticity but also, once yielding commences, allow the deformation to spread more extensively throughout the TPMS network before global buckling occurs. The augmented cross-sectional area provides greater resistance against the coalescence of localized plastic zones into a global instability, thereby enabling a larger volume of material to contribute to energy dissipation through plastic work. This explains why thicker specimens achieve substantially higher SEA values (up to 201% improvement) while also delaying the onset of buckling (from 1.73 mm to 2.16 mm). In essence, increasing thickness transforms the deformation mode from a plasticity-limited response to a plasticity-distributed response, simultaneously enhancing load capacity, energy absorption, and deformation stability.

To place the mechanical performance of the proposed TPMS framework into context, it is informative to compare its specific energy absorption with representative cylindrical polymer metamaterials reported in the literature. A recently developed cylindrical auxetic metamaterial fabricated using additive manufacturing achieved a maximum SEA of 231.6 mJ/g [50], while a tubular chiral metamaterial designed for automotive bumper applications reported SEA values exceeding 1300 mJ/g under quasi-static compression [51]. By comparison, the proposed gyroid TPMS architecture attained a maximum SEA of 3331 mJ/g, indicating a substantially higher energy absorption capability than these representative cylindrical metamaterial designs. Although direct quantitative comparisons should be interpreted with caution because of differences in unit-cell topology, relative density, material properties, and specimen geometry, these results nevertheless demonstrate the excellent energy absorption potential of the proposed TPMS architecture.

3.3. *Potential application in next-generation dental implants*

The proposed lightweight TPMS metamaterial framework may offer potential for future dental implant applications, see Fig. 9. Conventional solid metallic implants are known to exhibit a stiffness mismatch with

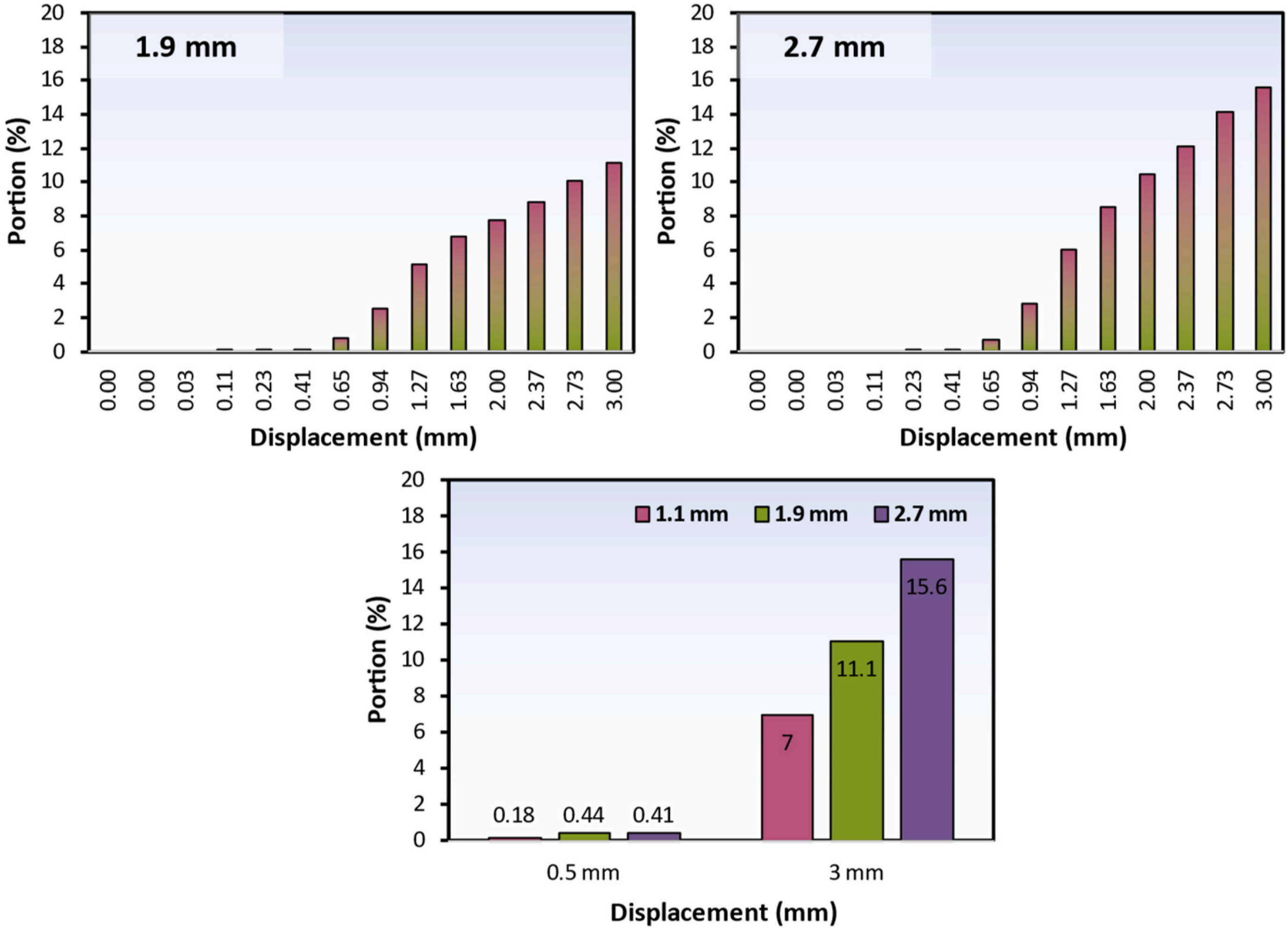

Fig. 8. Influence of unit-cell thickness for TPMS structure with constant three unit-cells arranged around one full circumference on the evolution of plastic deformation.

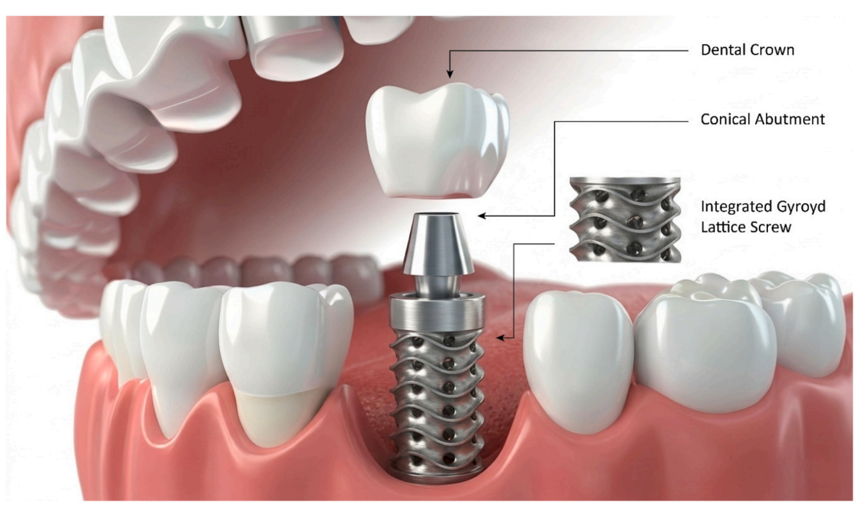

Fig. 9. Schematic illustration of the proposed lightweight TPMS metamaterial framework for dental implant applications.

surrounding bone, which has been associated with stress-shielding and bone resorption. The cylindrical gyroid architecture presented here allows for stiffness tunability by modifying either the wall thickness or the number of unit-cells per circumference (Table 1), suggesting the better matching the mechanical properties of cancellous bone. Furthermore, the porous nature of the TPMS structure could facilitate osseointegration through bone ingrowth and vascularization, although this remains to be validated through biological testing [52]. Nevertheless, the present study focuses exclusively on mechanical characterization and does not include permeability analyses, computational fluid dynamics, in vitro biological evaluations, or in vivo investigations. Therefore, the biological performance of the proposed framework remains to be established through future multidisciplinary studies before clinical translation can be considered. The specific energy absorption values obtained (up to 3331 mJ/g) indicate that the structure can dissipate mechanical energy, which may be relevant under masticatory loading conditions. Combined with the design flexibility offered by 3D printing, this metamaterial framework represents a candidate for further investigation toward patient-specific dental implant designs. It should be emphasized that the present investigation is intended as a proof-of-concept study to evaluate the mechanical influence of the proposed gyroid TPMS architecture rather than to reproduce the absolute mechanical behavior of a clinical dental implant. The photosensitive resin was selected because its high-resolution DLP printability enables the accurate fabrication of thin TPMS walls required for reliable experimental validation of the numerical model. Although the validated finite element model successfully captures the geometry-dependent deformation mechanisms of the proposed architecture, the constitutive behavior, yielding characteristics, and post-buckling response of the resin differ from those of clinically employed implant materials such as Ti-6Al-4V and zirconia. Consequently, the quantitative mechanical values reported in this study should not be interpreted as representative of metallic dental implants. Moreover, although the present study demonstrates favorable quasi-static mechanical performance of the proposed TPMS framework, dental implants are subjected to repetitive cyclic loading during mastication throughout their service life. Consequently, high-cycle fatigue behavior remains a critical aspect that has not been addressed in the current investigation. Also, it should be emphasized that the cylindrical specimens investigated in this study were intentionally selected to characterize the intrinsic mechanical response of the proposed TPMS framework under controlled conditions. They are not intended to represent the final geometry of a clinical dental implant. In practical applications, the TPMS architecture would be integrated within a threaded implant body to provide primary mechanical stability following implantation. The interaction between the external thread profile and the internal gyroid network is expected to influence local stress concentrations and load transfer. Therefore, future work will focus on incorporating clinically representative thread geometries into the proposed TPMS framework and evaluating their biomechanical performance through detailed finite element analyses and experimental validation along with experimental fatigue testing and fatigue-life prediction under physiologically relevant cyclic loading conditions to evaluate the long-term structural integrity and durability of the proposed architecture before clinical application can be considered.

4. Conclusions

This study introduced a novel cylindrical TPMS metamaterial based on a gyroid architecture, fabricated via 3D printing, and systematically investigated its compressive mechanical behavior through a combined experimental and numerical approach. A validated finite element model ($R^2 = 0.965$) was established using Abaqus, showing excellent agreement with quasi-static compression tests performed on specimens with a thickness of 1.9 mm and eleven unit-cells per circumference. The deformation mechanism was characterized by a distinct two-phase response: an initial elastic regime with no plastic deformation, followed by plasticity-driven global buckling initiating at the core between neighboring gyroid unit-cells. The main findings are summarized as follows.

- Two-phase deformation behavior was preserved across all geometric configurations, regardless of thickness or unit-cell count, confirming the robustness of the underlying TPMS architecture.
- Increasing unit-cell count (3 to 11) enhanced stiffness, peak load, and SEA but reduced instability displacement. Specific stiffness increased by 154% proving the improvement arises purely from topological reorganization, not material quantity.
- Increasing thickness simultaneously improved all mechanical metrics without compromising instability onset. This indicates that the thicker topology makes more efficient use of the added material rather than merely increasing it proportionally.
- Thickness variation proved more advantageous than unit-cell count adjustment, as it avoided the trade-off of earlier buckling while delivering superior improvements in load-bearing and energy absorption performance.
- The highest overall performance was achieved by the configuration with 2.7 mm thickness and eleven unit-cells, yielding a peak load of 3679.9 N, stiffness of 4495.2 N/mm, and SEA of 3331.0 mJ/g.

The tunable stiffness, high specific energy absorption, and inherent porosity of the proposed TPMS metamaterial suggest its potential for further investigation in load-bearing biomedical applications, subject to additional biocompatibility and fatigue testing.

Data availability statement

Not applicable.

Funding

This research received partial funding from Ajman University (2025-IRG-CEIT-2, 2025-IRG-CEIT-39) and the NWO (Dutch Research Council). The data essential for supporting the conclusions are presented within the paper.

Declaration of competing interest

The authors declare that they have no known competing financial interests or personal relationships that could have appeared to influence the work reported in this paper.

Acknowledgments

Not applicable.

References

[1] Rahimi H, Khajepour M, Rahmatabadi D, Faraji G, Baghani M, George D, Baniassadi M. Design, simulation, and experimental validation of metamaterials with direction-dependent stiffness. Alex Eng J 2026;134:460–72.
[2] Bodaghi M, Namvar N, Yousefi A, Teymouri H, Demoly F, Zolfagharian A. Metamaterial boat fenders with supreme shape recovery and energy absorption/dissipation via FFF 4D printing. Smart Mater Struct 2023;32(9):095028.
[3] Xue Y, Wang S, Song W. Design and mechanical performance of novel 3D enhanced isomorphic secondary hierarchical re-entrant auxetic structures fabricated by additive manufacturing. Thin-Walled Struct 2026:115107.
[4] Weidong S, Shi L, Shanshan L, Yuquan M, Runzhi L, Lijun X. Dynamic compressive response of twinning-inspired conformal lattices with constant relative density. Int J Impact Eng 2026:105694.
[5] Jaber A, Singh A, Rodopoulos DC, Karathanasopoulos N. Inner design and strain-rate effects on the performance of architected materials and interpenetrating phase composites: State-of-the-Art analysis and perspectives. Adv Eng Mater 2025;27(18):2500870.
[6] Yu G, Li X, Dai L, Xiao L, Song W. Compressive properties of imperfect Ti-6Al-4V lattice structure fabricated by electron beam powder bed fusion under static and dynamic loadings. Addit Manuf 2022;49:102497.
[7] Pai KR, Vijayan V, Prabhu KN. Investigation of the effect of process parameters on porosity, microstructure and mechanical properties of Al–5 Mg alloy test samples fabricated by wire arc additive manufacturing. Progr Addit Manuf 2025;10(8):4675–88.
[8] Gao W, Mai Y, Han W, Zhao S. Magneto-sensitive metamaterial with programmable in-plane actuation and tunable Poisson's ratio. Compos Struct 2026:120342.
[9] Khajepour M, Yousefi MA, Rahmatabadi D, Baghani M, Baniassadi M. Numerical and experimental characterization of 3D-Printed elliptical anti-chiral metamaterials with box-Behnken optimization. J Mater Res Technol 2026.
[10] Li Y, Han X, Ma Z. Research on the mechanical properties of PEEK material artificial bone implants fabricated by high-temperature air-assisted 3D printing. J Mech Behav Biomed Mater 2025:107207.

[11] Lin C, Yang M, Zhang F, Liu Y, Leng J. Stimuli-responsive smart materials for biomedical applications. Mater Sci Eng R Rep 2026;167:101126.
[12] Lin C, Yang M, Chen K, Liu Y, Liu F, Zou Z, Zhang X, Xin X, Huang J. 4D-Printed sandwich-structured metamaterial intestinal stents for palliative tumor therapy. Adv Mater 2026;38(32):e18990.
[13] Wang J, Li S, Liu L, Liu F, Lin C, Liu Y, Leng J. 4D-Printed intelligent reconfigurable occluder with anti-thrombotic and rapid-repairing capabilities for patent foramen ovale. Adv Healthcare Mater 2026:e05214.
[14] Hao X, Jiang B, Wu J, Xiang D, Xiong Z, Li C, Li Z, He S, Tu C, Li Z. Nanomaterials for bone metastasis. J Contr Release 2024;373:640–51.
[15] Zhang S, Xu Z, Zhang W, Xu C, Li Y, Zhang Y, Xu J, Peng F, Shen L, Wu Z. High-strength and ductile TiNbZrTa BCC MPEA with heterogeneous microstructure for orthopedic implants. Adv Healthcare Mater 2026:e05213.
[16] Lin H, Yin X, Wang Z, Xu J, Wang Y, Cheng S, Yang J, Wang Y. Friction-induced PTFE coating on dental restorative resin with ultralow friction and wear. Langmuir 2025;41(33):22501–6.
[17] Tang H, Wang H, Sun W, Chen Y, Pan Z, Bai Q, Wang Y, Lin W, Hu Y, Wang L. A bio-adaptive physical hydrogel enables dynamic tissue engineering for tracheal reconstruction. Nat Commun 2025.
[18] Wakjira Y, Cioni A, Lemu HG. Current status of the application of additive-manufactured TPMS structure in bone tissue engineering. Progr Addit Manuf 2025; 10(2):1085–102.
[19] Dang HL, Tran NH, Luong VH. Geometrically nonlinear dynamic analysis of FG-TPMS plates on a pasternak foundation subjected to moving loads using the MEM method. Int J Struct Stabil Dynam 2026.
[20] Chen X. Exploring fillet radius effects in 3D-printed Schwarz triple periodic minimal Surface (TPMS) structures: experimental validation and FEM insights. Mech Base Des Struct Mach 2026;54(1):2623520.
[21] Lu Y, Hao B, Li G, Zheng H, Zhang L. Investigation of the ballistic resistance of the triply periodic minimal surface lattice-structured wing fabricated via 3D printing. Mech Base Des Struct Mach 2026:1–28.
[22] Babaei H, Zavari S, Kaveh A, Arshid E, Civalek Ö. Dynamic response of advanced lightweight porous plates integrated with nanocomposite face sheets resting on elastic substrate. Int J Struct Stabil Dynam 2025;25(12):2550132.
[23] Kapfer SC, Hyde ST, Mecke K, Arns CH, Schröder-Turk GE. Minimal surface scaffold designs for tissue engineering. Biomaterials 2011;32(29):6875–82.
[24] Abueidda DW, Elhebeary M, Shiang C-SA, Pang S, Al-Rub RKA, Jasiuk IM. Mechanical properties of 3D printed polymeric Gyroid cellular structures: experimental and finite element study. Mater Des 2019;165:107597.
[25] Maskery I, Aboulkhair NT, Aremu AO, Tuck CJ, Ashcroft IA. Compressive failure modes and energy absorption in additively manufactured double gyroid lattices. Addit Manuf 2017;16:24–9.
[26] Yang E, Leary M, Lozanovski B, Downing D, Mazur M, Sarker A, Khorasani A, Jones A, Maconachie T, Bateman S. Effect of geometry on the mechanical properties of Ti-6Al-4V Gyroid structures fabricated via SLM: a numerical study. Mater Des 2019;184:108165.
[27] Dziaduszewska M, Zieliński A. Structural and material determinants influencing the behavior of porous Ti and its alloys made by additive manufacturing techniques for biomedical applications. Materials 2021;14(4):712.
[28] Gaviria L, Salcido JP, Guda T, Ong JL. Current trends in dental implants. Journal of the Korean Association of Oral and Maxillofacial Surgeons 2014;40(2):50.
[29] Rho JY, Ashman RB, Turner CH. Young's modulus of trabecular and cortical bone material: ultrasonic and microtensile measurements. J Biomech 1993;26(2):111–9.
[30] Mi ZR, Shuib S, Hassan A, Shorki A, Ibrahim M. Problem of stress shielding and improvement to the hip Implat designs: a review. J Med Sci 2007;7(3):460–7.
[31] Sumitomo N, Noritake K, Hattori T, Morikawa K, Niwa S, Sato K, Niinomi M. Experiment study on fracture fixation with low rigidity titanium alloy: plate fixation of tibia fracture model in rabbit. J Mater Sci Mater Med 2008;19(4): 1581–6.
[32] Arabnejad S, Johnston RB, Pura JA, Singh B, Tanzer M, Pasini D. High-strength porous biomaterials for bone replacement: a strategy to assess the interplay between cell morphology, mechanical properties, bone ingrowth and manufacturing constraints. Acta Biomater 2016;30:345–56.
[33] Wang X, Xu S, Zhou S, Xu W, Leary M, Choong P, Qian M, Brandt M, Xie YM. Topological design and additive manufacturing of porous metals for bone scaffolds and orthopaedic implants: a review. Biomaterials 2016;83:127–41.
[34] Bobbert F, Lietaert K, Eftekhari AA, Pouran B, Ahmadi S, Weinans H, Zadpoor A. Additively manufactured metallic porous biomaterials based on minimal surfaces: a unique combination of topological, mechanical, and mass transport properties. Acta Biomater 2017;53:572–84.
[35] Imanian ME, Kardan-Halvaei M, Nasrollahi F, Imanian A, Montazerian H, Nasrollahi V. 3D printed flexible wearable sensors based on triply periodic minimal surface structures for biomonitoring applications. Smart Mater Struct 2022;32(1): 015015.
[36] Song K, Wang Z, Lan J, Ma S. Porous structure design and mechanical behavior analysis based on TPMS for customized root analogue implant. J Mech Behav Biomed Mater 2021;115:104222.
[37] Keshishian T, Salami SJ, Geramizadeh H, Keshishian A, Dariushi S. Manufacturable design and experimental investigation of functionally graded TPMS-based root analogue implant for dental applications. Results Eng 2026:109574.
[38] Yan C, Hao L, Hussein A, Young P. Ti–6Al–4V triply periodic minimal surface structures for bone implants fabricated via selective laser melting. J Mech Behav Biomed Mater 2015;51:61–73.
[39] Moghariya J, Gurrala PK. Finite element studies on triply periodic minimal surfaces (TPMS)–based hip replacement implants. Int J Adv Manuf Technol 2025;136(1): 263–77.
[40] Dyer K, Amjadi M, Shao S, Shamsaei N, Molaei R. Understanding fatigue of additively manufactured TPMS metallic metamaterials: experiments and modeling. Addit Manuf 2025:104966.
[41] Žnidarič Ž, Nečemer B, Novak N, Vesenjak M, Glodež S. Fatigue of triply periodic minimal surface (TPMS) metamaterials–A review. Strojniški vestnik-Journal of Mechanical Engineering 2025;71(9–10):357–68.
[42] Xu Z, Sarkar A, Hayes AC, Branco R, Wronski S, Tarasiuk J, Borrego L, Razavi N. Geometric determinants of monotonic and fatigue performance in additively manufactured TPMS lattice structures: decomposing scale effects. Mater Des 2026: 116431.
[43] Abdelgawad A, Barsoum I, Al-Rub RKA. An integrated computational modeling framework for predicting fatigue crack growth in additive manufactured TPMS structures. Int J Fatig 2026:109749.
[44] Kadkhodapour J, Montazerian H, Darabi AC, Zargarian A, Schmauder S. The relationships between deformation mechanisms and mechanical properties of additively manufactured porous biomaterials. J Mech Behav Biomed Mater 2017; 70:28–42.
[45] Xia X, Chen X, Zhang Z, Chen X, Zhao W, Liao B, Hur B. Effects of porosity and pore size on the compressive properties of closed-cell Mg alloy foam. J Magnesium Alloys 2013;1(4):330–5.
[46] Ren H, Shen H, Ning J. Effect of internal microstructure distribution on quasi-static compression behavior and energy absorption of hollow truss structures. Materials 2020;13(22):5094.
[47] Laskowska D, Szatkiewicz T, Bałasz B, Mitura K. Mechanical properties and energy absorption abilities of diamond TPMS cylindrical structures fabricated by selective laser melting with 316L stainless steel. Materials 2023;16(8):3196.
[48] Standard I. ISO 13314: 2011 (E)(2011) mechanical testing of metals—ductility testing—compression test for porous and cellular metals. 2011. p. 1–7. Ref number ISO 13314(13314).
[49] Sun Q, Sun J, Guo K, Liu J. Investigation on mechanical properties and energy absorption capabilities of AlSi10Mg triply periodic minimal surface sheet structures fabricated via selective laser melting. J Mater Eng Perform 2022;31(11): 9110–21.
[50] Zhu M, Habibi M. Influence of unit cell parameters on mechanical characteristics of 3D-Printed cylindrical metamaterial structure: a finite element and experimental study. Adv Eng Mater 2026:e202502899.
[51] Guo W, Zhou M. Design and experimental validation of additive manufactured cylindrical metamaterials for load-bearing automotive bumper. Mech Base Des Struct Mach 2026;54(1):2666599.
[52] Liu H, Chen H, Zhao X, Sun B, Xu C, Zhang A, Liu Y, Wei H, Wang Z, Han Q. Curvature-guided TPMS scaffolds: a metamaterial design framework for osteogenic microenvironments. Thin-Walled Struct 2025:114171.